



HAL
open science

Prediction of the Onset of Heavy Rain Using SEVIRI Cloud Observations

Maximilien Patou, Jérôme Vidot, J. Riedi, Guillaume Penide, Timothy
Garrett

► **To cite this version:**

Maximilien Patou, Jérôme Vidot, J. Riedi, Guillaume Penide, Timothy Garrett. Prediction of the Onset of Heavy Rain Using SEVIRI Cloud Observations. *Journal of Applied Meteorology and Climatology*, 2018, 57 (10), pp.2343-2361. 10.1175/JAMC-D-17-0352.1 . hal-03496954

HAL Id: hal-03496954

<https://hal.science/hal-03496954>

Submitted on 28 Dec 2021

HAL is a multi-disciplinary open access archive for the deposit and dissemination of scientific research documents, whether they are published or not. The documents may come from teaching and research institutions in France or abroad, or from public or private research centers.

L'archive ouverte pluridisciplinaire **HAL**, est destinée au dépôt et à la diffusion de documents scientifiques de niveau recherche, publiés ou non, émanant des établissements d'enseignement et de recherche français ou étrangers, des laboratoires publics ou privés.



Distributed under a Creative Commons Attribution 4.0 International License

Prediction of the Onset of Heavy Rain Using SEVIRI Cloud Observations

MAXIMILIEN PATOU

Université de Lille, CNRS, UMR 8518-LOA-Laboratoire d'optique Atmosphérique, F-5900 Lille, France

JÉRÔME VIDOT

Centre de Météorologie Spatiale, Météo-France, Lannion, France

JÉRÔME RIÉDI AND GUILLAUME PENIDE

Université de Lille, CNRS, UMR 8518-LOA-Laboratoire d'optique Atmosphérique, F-59000 Lille, France

TIMOTHY J. GARRETT

Department of Atmospheric Sciences, University of Utah, Salt Lake City, Utah

(Manuscript received 18 December 2017, in final form 23 July 2018)

ABSTRACT

Thunderstorms and strong precipitation events can be highly variable in space and time and therefore are challenging to forecast. Geostationary satellites are particularly well suited for studying their occurrence and development. This paper describes a methodology for tracking temporal trends in the development of these systems using a combination of a ground-based radar rainfall product and cloud fields derived from the Meteosat Second Generation's (MSG) Spinning Enhanced Visible and Infrared Imager (SEVIRI). Cloud microphysical and radiative properties and the cloud perimeter-to-area ratio are used to characterize the temporal evolution of 35 cases of isolated convective development. For synchronizing temporal trends between cases, two reference times are used: the time when precipitating clouds reach a rain intensity threshold and the time of the maximum of rain intensity during the cloud life cycle. A period of decreasing cloud perimeter-to-area ratio before heavy rainfall is observed for both synchronization techniques, suggesting this parameter could be a predictor of heavy rain occurrence. However, the choice of synchronization time does impact significantly the observed trend of cloud properties. An illustration of how this approach can be applied to cloud-resolving models is presented to evaluate their ability to simulate cloud processes.

1. Introduction

Heavy rainfall associated with hail and flash flooding can have devastating impacts on a broad range of human activities (Adachi et al. 2013). Accurate short-range forecasts of thunderstorms are necessary to provide the public with early warnings of these events (Zinner et al. 2008). Researchers looking at convective cloud systems in past decades have applied a range of approaches to track and characterize their evolution for the purpose of short-range forecasting (nowcasting) (Sieglaff et al. 2011), thunderstorm classification (Cintineo et al. 2013), mesoscale convective system (MCS) life cycle

characterization (McAnelly and Cotton 1989; Roca et al. 2017), and cumulonimbus detection (Henken et al. 2011).

MCS detection using meteorological satellites (Machado et al. 1998; Carvalho and Jones 2001; Vila et al. 2008) usually relies upon identifying regions where the infrared brightness temperature passes a threshold generally below 241 K (Maddox 1980). An area overlapping technique (Mathon and Laurent 2001) has been applied recently at high temporal resolution to track the rapid evolution of convective areas (Liu et al. 2015). While such tracking techniques have mostly been applied to tropical areas, they have also been successfully extended to the midlatitudes (Morel and Senesi 2002a; Kolios and Feidas 2013). Machado and Laurent (2004) used a similar tracking technique to show a maximum in cloud-area expansion of tropical MCS close to the time of maximum precipitation.

Corresponding author: Maximilien Patou, maximilien.patou@ed.univ-lille1.fr

DOI: 10.1175/JAMC-D-17-0352.1

© 2018 American Meteorological Society. For information regarding reuse of this content and general copyright information, consult the [AMS Copyright Policy](#) (www.ametsoc.org/PUBSReuseLicenses).

Such studies remain, however, limited to the MCS life cycle and to deep convection analysis.

Other studies have looked at specific stages of cloud development for nowcasting applications. Using the Spinning Enhanced Visible and Infrared Imager (SEVIRI) infrared 10.8- μm , water vapor (infrared 6.2- μm), and visible and high-resolution visible (HRV) channels, Zinner et al. (2008) focused on cumulonimbus cloud at midlatitudes to develop the so-called Cumulonimbus Tracking and Monitoring (Cb-TRAM) algorithm. In Cb-TRAM, temporal information and SEVIRI channel thresholds are used to define the stages of cloud development. This method identifies convective initiation from the temporal variation of cloud area in HRV imagery and cooling in the water vapor channel. Other convective and storm initiation nowcasting methodologies are based on relative cooling rates of developing convective cells during the early stages of development (Roberts and Rutledge 2003; Mecikalski and Bedka 2006; Mecikalski et al. 2008, 2010a,b; Sieglaff et al. 2011, 2014; Mecikalski et al. 2015). The time of convective initiation as defined by the first occurrence of a radar reflectivity greater than 35 dBZ (Roberts and Rutledge 2003; Mecikalski and Bedka 2006) is used as a reference time for cloud property temporal analyses. Mecikalski et al. (2011) studied trends in cloud effective radius (REFF), cloud optical thickness (COT), and cloud-top pressure for a 30-min period 15–45 min before convective initiation. They observed that, as cumuli deepen, COT values increase and cloud-top pressure decreases but that trends in REFF are not monotonic.

Satellite-derived cloud properties such as REFF, COT, cloud-top thermodynamic phase, and cloud-top temperature (CTT) have also been used by several authors to analyze convective cloud evolution. Lensky and Rosenfeld (2006, 2008) and Rosenfeld et al. (2008) showed a correlation between CTT and REFF as a function of aerosol content and updraft strength. Cintineo et al. (2013) studied two classes of storm (severe and nonsevere) and showed that temporal trends of these parameters can be used to extend severe-weather-warning lead times. Senf et al. (2015) compared SEVIRI COT and ice REFF retrievals with cloud anvil edge velocity and average cloud-top vertical velocities. They used the time of maximum cloud-top cooling rate for temporal synchronization to extract temporal trends from nine study cases. Their analysis of REFF retrievals showed that larger ice crystal REFF values are present for clouds tops with lower vertical velocities. This work also showed that the rate of spread of cloud anvils provides information on the strength of convective updrafts. This analysis was recently extended to more than 100 cloud anvil cases (Senf and Deneke 2017a), confirming that smaller ice

crystal REFF values occur during strong rainfall periods and that high radar reflectivities occur before the time of the maximum in the cloud-top cooling rate. Moreover, cloud morphology was also studied, especially cloud perimeter P and cloud area A . Perimeter and area data have been used to estimate the fractal dimension D of regions with clouds and rain (Lovejoy 1982). On average, $P \propto A^{D/2}$, where $D \simeq 4/3$, although Batista-Tomás et al. (2016) showed that the fractal dimension changes over the course of a transition from cumulonimbus to cirrus. The A/P ratio was directly introduced by Vila and Machado (2004) and interpreted as the compactness of cloud to characterize the shape and internal structure of convective systems.

The aforementioned studies highlight that temporal analysis of cloud-top morphology, cloud-top microphysics, and radiative properties can be used to characterize the development of convective clouds. However, many of these studies have not included a combined temporal analysis of precipitation at the ground and cloud-top observations from geostationary satellites. We propose in this work an approach to analyze precipitating-cloud development from geostationary satellite-based and ground-based radar data observations. In particular, we propose a combined analysis of temporal trends in REFF, COT, CTT, cloud-top phase, the cloud perimeter-to-area ratio (CPAR), and the maximum of rainfall values at the ground. The objective is to evaluate whether the evolution of cloud parameters derived from geostationary satellites carries information that could be used to anticipate the onset of heavy precipitation. The data used in this study, the tracking methods, and the case study selection are described in section 2. We present in section 3 a temporal analysis of 35 study cases and discuss a preliminary illustration of how such analyses could be used to evaluate cloud-resolving models. Conclusions, limitations of this approach, and future prospects are provided in section 4.

2. Observational data

a. Data and products

For our analyses, we use data from SEVIRI onboard the geostationary Meteosat Second Generation (MSG) satellites (Schmetz et al. 2002). A high temporal resolution is necessary to resolve finer details in convective cloud development (Adler and Fenn 1979; Cintineo et al. 2013). For this, we use the Rapid Scan Service (RSS) of SEVIRI, which provides a 5-min temporal resolution and a spatial resolution over France of approximately 4–5 km. From these high temporal resolution observations we generate a cloud mask (CM), a cloud typing (CT), and four parameters describing

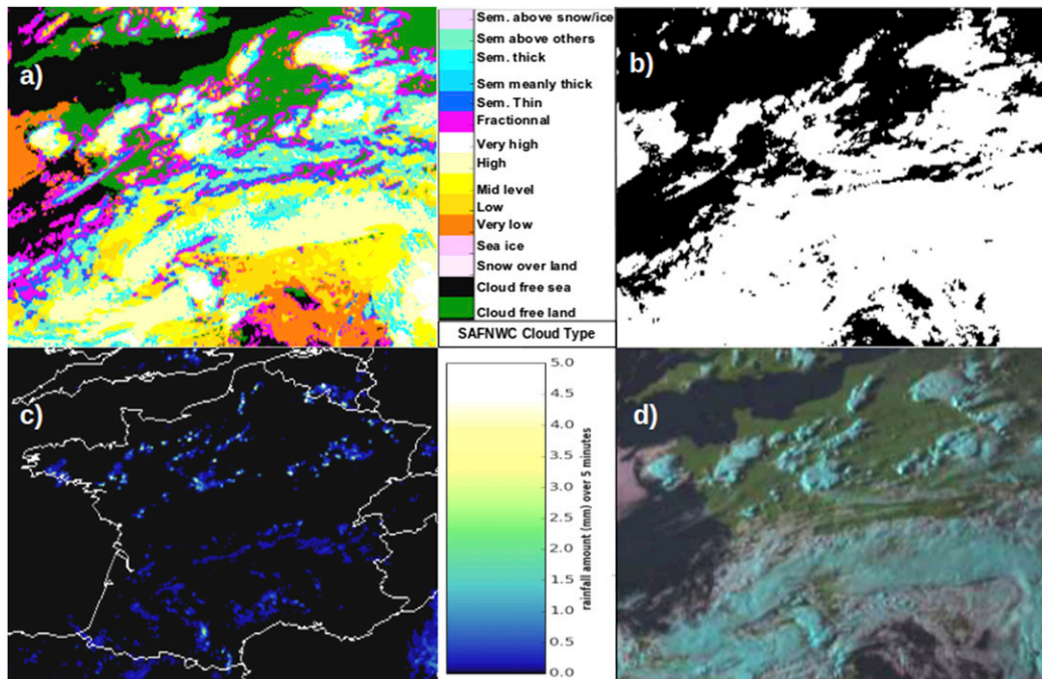


FIG. 1. (a) SAFNWC cloud-type product, (b) cloud mask generated with selection of all cloud types excluding fractional clouds, (c) PANTHERE accumulated rain over 5 min projected onto the SEVIRI RSS grid, and (d) EUMETSAT red–green–blue (RGB) natural color image following the Rosenfeld et al. (2008) method. All data are at 1630 UTC 23 Apr 2011.

cloud properties (REFF, COT, CTT, and the cloud-top phase). Cloud detection and typing are obtained using the European Organisation for the Exploitation of Meteorological Satellites (EUMETSAT) Satellite Application Facility on Support to Nowcasting and Very Short Range Forecasting (SAFNWC) cloud-mask and cloud-type product as described by Derrien and Le Gléau (2005, 2010). The algorithms use multispectral thresholding techniques to detect cloudy pixels and classify clouds. An example of the SAFNWC cloud type product over France is shown in Fig. 1a. Our cloud tracking method uses a simple binary mask (cloud cover of interest) to detect cloud shape and area. This binary mask (Fig. 1b) is a selection of all cloud types excluding the fractional clouds corresponding to partially cloudy pixels (represented in pink in Fig. 1a).

Two algorithms are used to provide REFF, COT, CTT, and cloud-top phase. The 2016 version of the SAFNWC package software (Le Gléau 2016) is used to retrieve CTT and cloud types in this study. For REFF and COT values, we used visible–infrared 1.6- μm retrievals from the SEV06-CLD cloud product distributed by ICARE/AERIS (2017). The SEV06-CLD product is an adaptation for SEVIRI of the operational Collection 6 MODIS (MOD06/MYD06) cloud optical and microphysical retrieval algorithm (Platnick et al. 2001,

2003, 2017) and the *GOES-16* cloud-top properties algorithm (Heidinger and Pavolonis 2009; Heidinger et al. 2010). The latest microphysical and optical assumptions for ice clouds assumed in the of MODIS Collection 6 algorithm are used in SEV06-CLD. For ice crystals, a gamma size distribution consisting of severely roughened compact aggregated columns is used (Platnick et al. 2017). The SEV06-CLD algorithm, similar to the MODIS algorithm, follows the approach of Nakajima and King (1990) to infer COT and REFF. This approach uses lookup table of precalculated reflectance pairs in the visible (0.6 and 0.8 μm) and near-infrared (1.6 μm) spectra for discrete values of COT and REFF. The reflectance in the visible range is mainly sensitive to optical thickness while the reflectance at 1.6 μm is affected by water/ice particle absorption, and therefore carries information on the particle size and thermodynamic phase. Cloud-top phase information is retrieved by using an infrared bispectral method adapted for SEVIRI similar to the method described in Platnick et al. (2003). A similar method has been evaluated previously by Wolters et al. (2008) using SEVIRI observations, ground-based lidar, and cloud radar data. Because of the daytime limitation of SEV06-CLD COT and REFF retrievals, we have only used data collected when the SEVIRI solar zenith angle $\leq 70^\circ$. Note also that because

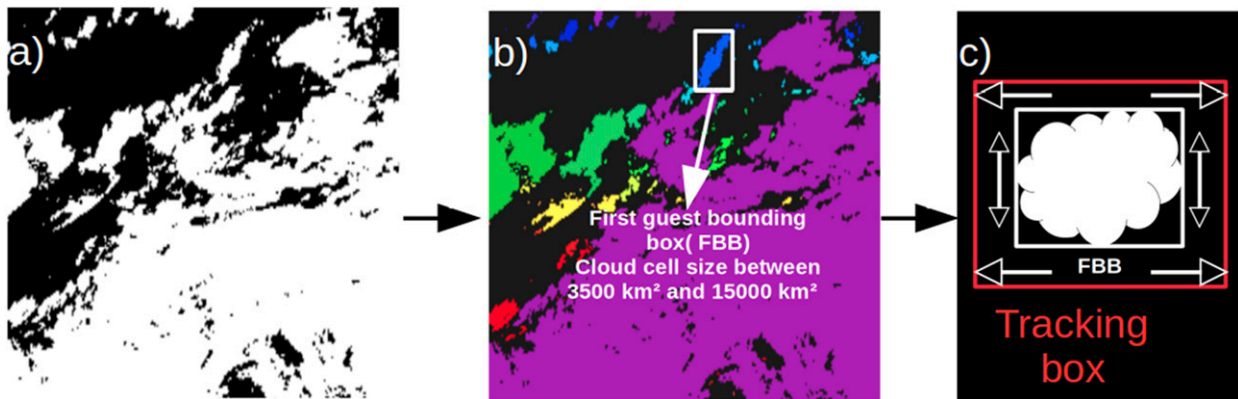


FIG. 2. Schematic view of the detection of an isolated cloud during daytime. Example at 1600 UTC 23 Apr 2011 of isolated cloud detection under fair weather conditions and the box-area determination method for tracking the cloud. (a) Cloud cover colored in white considered in the tracking procedure. (b) Labeled image to detect cloud objects and first bounding box (FBB) detection of isolated cloud. (c) Increase of the FBB to define the tracking box where the tracking is performed.

of SEVIRI's coarser spatial resolution compared to MODIS, the COT and REFF retrievals are more prone to biases in cases of heterogeneous cloud cover (Zhang and Platnick 2011; Zhang et al. 2012).

To provide an estimate of rainfall intensity during the cloud life cycle, we have used the Météo-France rain accumulation PANTHERE (Programme Aramis Nouvelles Technologies en Hydrométéorologie Extension et Renouvellement) product (Tabary 2007) that is based on the French ground-based radar network. This product has the same temporal resolution (5 min) as SEVIRI RSS and provides an accumulation of rain over the past 5 min at a spatial resolution of 1 km. The PANTHERE product is based on a conversion of reflectivity Z to rain rate R using a Z - R -like relationship corrected for partial beam blocking and other artifacts (Tabary 2007). Derivation of a 5-min rain accumulation is made by using a cross-correlation advection field to mitigate undersampling effects. Details, improvement, and validation against rain gauges can be found in Tabary (2007), Tabary et al. (2007), Renard et al. (2012), and Figueras i Ventura and Tabary (2013). Collocation of the PANTHERE product with SEVIRI cloud products is performed by simple aggregation of rain data into the nearest neighbor SEVIRI grid to obtain spatially coherent information (Fig. 1c). Here, we limit our analysis to an area over France (Figs. 1a–d) due to the PANTHERE product availability. EUMETSAT red–green–blue (RGB) false-color composite imagery (Fig. 1d) is used as a complement to manually analyze the presence of clouds and clear-sky conditions for the 35 cases studied in section 3.

b. Cloud object tracking methodology

We wish to establish the history leading up to a precipitation event by considering the development of the

entire cloud system, without needing to specify a priori a temperature threshold. We have developed a cloud tracking method specifically designed to estimate cloud perimeter corresponding to the interface between isolated clouds and their clear-sky surroundings. In this method, we avoid the use of a specific CTT criterion as much as possible to include analysis of the pre-convective environment and the period without precipitation. This method is not designed to detect convective clouds but to analyze mean cloud-top properties of the SEV06-CLD product and cloud morphology on specific periods of precipitation intensification. For this, we tried to remain as general as possible in our cloud selection and only discard the fractional cloud type of the SAFNWC product: fractional cloud type pixels represent difficult borderline cases for cloud detection and there are generally no retrievals of COT, REFF, CTT, and cloud-top phase where there is broken cloud cover.

Our cloud object tracking method is based on automatic overlap and segmentation techniques performed in three steps. The first step identifies the cloud cover considered in our tracking technique, the second step is devoted to the tracking procedure, and the last step establishes a quality index for the tracking. Starting from the cloud cover shown in Fig. 1b and reproduced in Fig. 2a, we make a distinction between each cloud cell at each time step by applying a connected-component labeling algorithm for binary mask inputs available in the Scikit-image Python library (Wu et al. 2005; van der Walt et al. 2014). This algorithm allows us to detect cloud objects. When a detected cloud cell object reaches a size range between 3500 and 15 000 km², a first-guess bounding box (FBB) is defined around that object. The size of this bounding

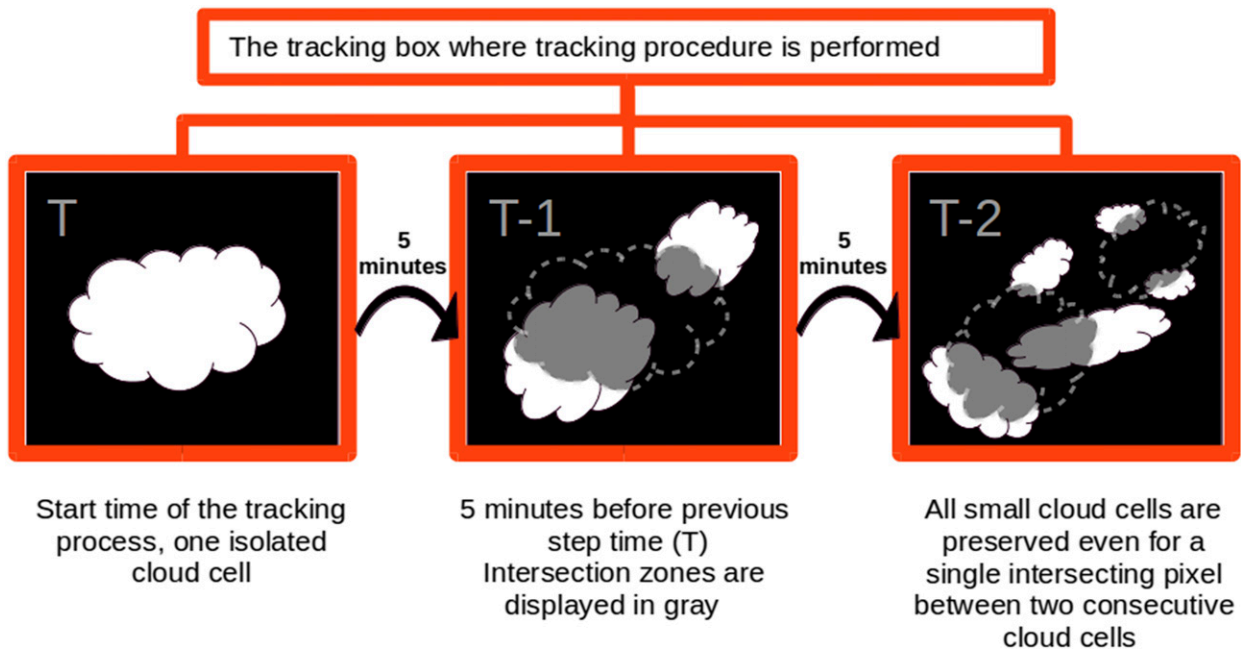


FIG. 3. Schematic view of the area-overlap-based tracking method. The tracking procedure is performed in the time-invariant tracking box. The reverse chronological order is used to determine cloud-system evolution. This tracking technique is limited to cloud systems surrounded by clear sky within the tracking box.

box is increased by 15 pixels in all directions to define a tracking box represented on Fig. 2c. The choice of a 3500–15 000-km²-area range is inspired by Morel and Senesi, although where Morel and Senesi (2002b) used an area of 1000–10 000 km² to track MCS systems over France, we expanded this area to consider both the cloud system and its clear-sky surroundings.

The second step consists of temporally connecting all cloud cells. This is performed using an area-overlap-based technique for successive images similar to previous studies (Mathon and Laurent 2001; Zinner et al. 2008; Liu et al. 2015). Because SEVIRI RSS data have a short refresh period of 5 min this approach is especially efficient (Liu et al. 2015). Clouds can be tracked in successive images provided there is an intersection of their areas. However, as explained by Arnaud et al. (1992), a cloud does not generally stay as a single connected object during a tracking procedure. Using the largest intersection surface between two successive images can artificially reduce the cloud system apparent lifetime (Mathon and Laurent 2001).

To address these concerns, we have adopted a cloud tracking strategy where we first analyze cloud evolution by searching backward in time (i.e., two consecutive images correspond to an image at time T and an image at time $T - 5$ min). Second, the tracking procedure is initiated and performed only within the tracking box defined in the detection procedure (Fig. 2c). The tracking

box is a time-invariant area and sets the boundaries where the cloud is tracked. A reverse chronological order is used to track a cloud object among the entire set of objects detected within the tracking box during the daytime. As shown in Fig. 3, dashed lines indicate the previous location of cloud cells, and gray areas correspond to the overlap between adjoining time steps. A cloud object is preserved even for a single intersecting pixel between two consecutive cloud cells so as to increase the duration of the tracking period.

The use of a fixed tracking box to track clouds comes from a trade-off between a need to detect cloud system development within the clear surroundings and a desire for a tracking technique that does not rely on the detection of convective clouds based on CTT criteria. The time of the tracking box corresponds to the time at which the cloud object reaches the size range between 3500 and 15 000 km². It is important to keep in mind that we use a reverse chronological order to track cloud systems. Therefore, this time corresponds to the beginning of the tracking procedure and the latest moment of cloud development on the period analyzed. The size range criterion is only applied at this specific time and not imposed at other time steps.

Our tracking method is designed to detect complex situations when a cloud object outside of the tracking box extends across the tracking-box border to contaminate the interior of the tracking area. To deal with these

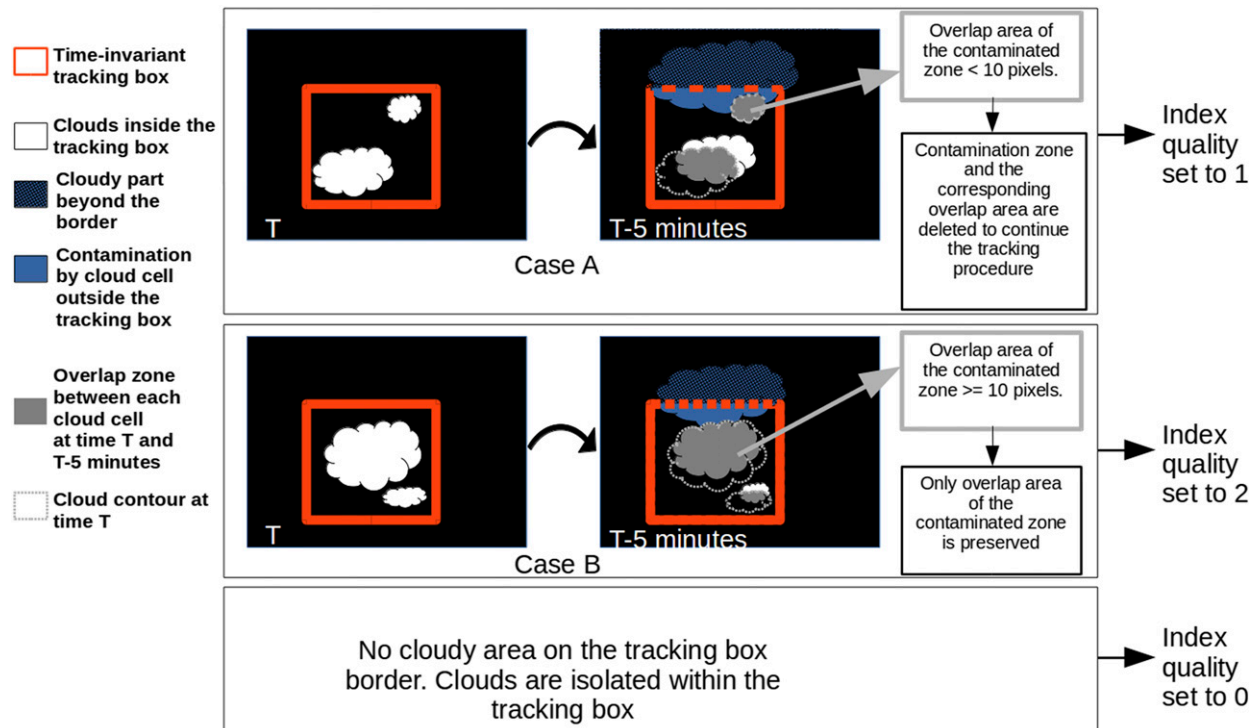


FIG. 4. Complex situations with cloud contamination on the border of the tracking box. (top) Case A: A small tracked cloud cell overlaps with another large size cloud cell outside the tracking box. (bottom) Case B: The cloud mask used as input classifies a large cloud cell within the tracked cloud set and a large cloud cell outside the tracking box as the same cloud object. A threshold of intersection area (gray) between the cloud object at time T and the cloud contamination at time $T - 5$ min on the tracking-box border (blue area) is used to continue to track the cloud cell.

situations, we consider the number of intersecting pixels between two consecutive cloud cells (Fig. 4). A threshold of 10 pixels of overlap between consecutive cloud objects categorizes these cases as either case A for an overlap area less than 10 pixels or case B for an overlap area greater than or equal to 10 pixels. Classification as either case A or B is done for each time step and for all clouds straddling the edges of the tracking box. Once these clouds are classified, they are deleted entirely for case A (Fig. 4, case A), or their corresponding overlap areas are preserved for case B (Fig. 4, case B). The occurrence of clouds near the borders of the tracking box tends to be temporary and we continue to track clouds even for these complex situations.

As a final step, an index for tracking quality is defined at each time step. It is set to zero in the absence of clouds on the edges of the tracking box, to 1 if there is at least one instance of case A and no case B, or to 2 if at least one case B is detected. A tracking quality index of zero indicates local, isolated clouds development and weak displacement in the tracking box. We want to highlight that the tracking box and quality index definitions are

only designed to detect isolated cloud systems when cloud perimeter can be computed. The tracking quality index is useful to estimate the quality of perimeter, area, or CPAR estimates. A quality index greater than 1 indicates that we have poor quality of these estimates. However, the tracked box is not adapted to study cloud systems associated with the fastest horizontal displacement.

c. Case study selection and classification

A tracked cloud is automatically flagged as “valid” and selected if the tracking duration is greater than 2 h (Fig. 5a). Tracked clouds identified as being valid do not contribute to another cloud tracking. Cloud perimeter is then estimated in pixel number from the binary cloud mask. Perimeter estimation is converted to kilometers using a fixed pixel length of 4.5 km, which provides a reasonable estimate, especially given that it is perimeter temporal trends that are considered. The cloud perimeter-to-area ratio (CPAR) is defined as P/A , where P and A are, respectively, the total perimeter and the total area for the tracked cloud objects in the tracking box. REFF, COT, cloud phase, CTT,

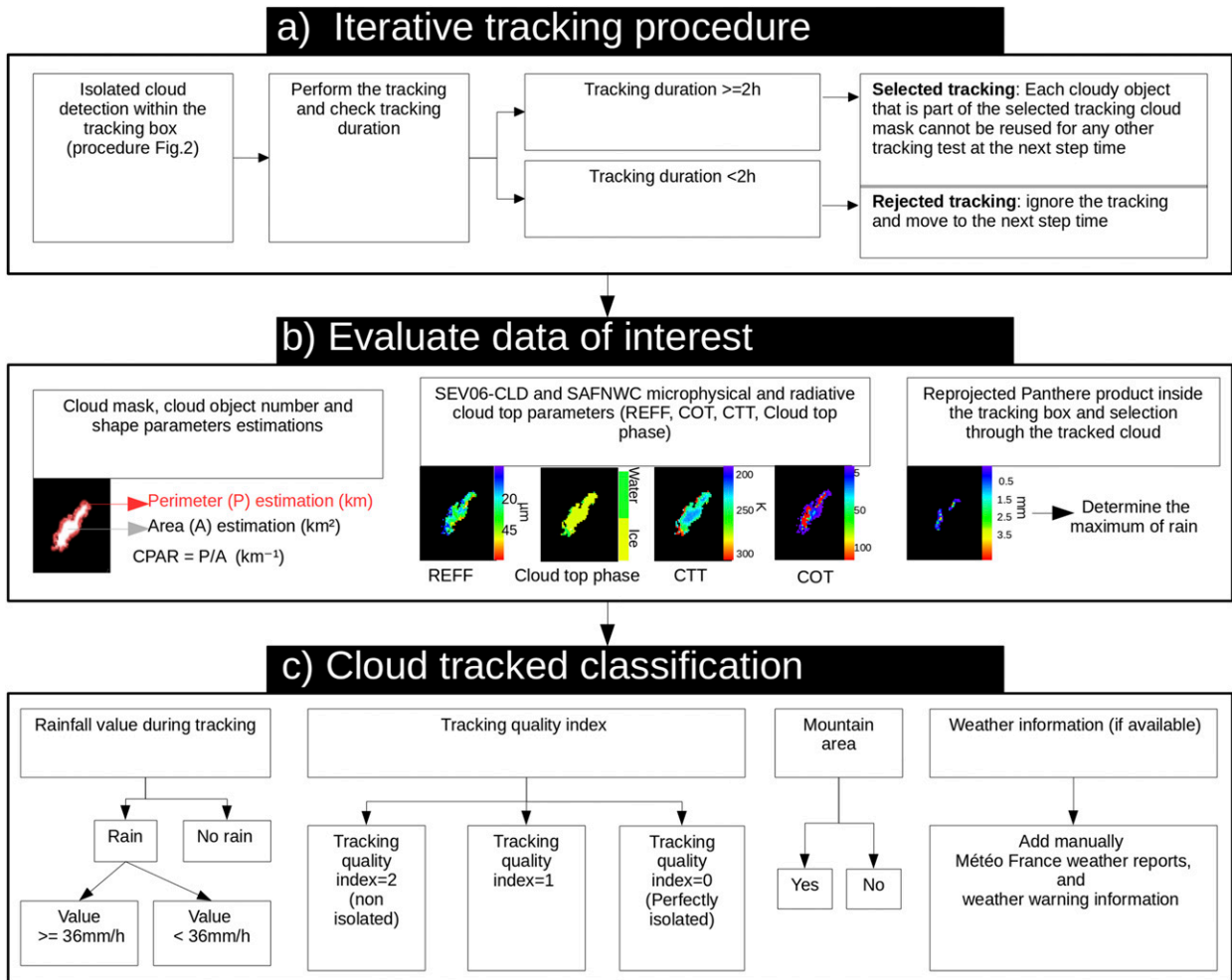


FIG. 5. Automatic cloud tracking selection and classification; only weather information is added manually.

CPAR, and the maximum of rain for each time step are evaluated for tracked clouds (Fig. 5b). The maximum of precipitation is converted for further analysis to units of millimeters per hour. Classification of tracked cloud objects is made based on the occurrence and amount of rain, the quality index, and the local orography (Fig. 5c). We identify tracked clouds with a rain accumulation >3 mm over 5 min and with quality index values of zero as “strong isolated rainfall events” separately from other rainy events. All tracked cloud systems with an index quality different from 0 corresponding to non-isolated cloud systems are filtered to study only cloud morphology of isolated cloud systems surrounded by clear sky. We selected 35 case studies over France using the method described in Fig. 5. Figure 6 shows the locations of the tracking boxes for the selected cases.

Daily weather reports and weather regional warnings from Météo-France were analyzed to confirm the presence

of storms in tracked-cloud-system regions. (See the appendix for details.)

3. Temporal analysis of case studies over France

a. Reference time synchronization based on the rainfall product

Because the tracked systems we consider have different lifetimes and occur at different times of the day, it is necessary to synchronize them to an arbitrary reference time in order to obtain a statistical representation of their life cycle. The choice of this reference time is particularly important as it impacts our ability to highlight temporal behavior around specific stages of cloud development.

Two times are defined to synchronize the evolution of each of the 35 tracked clouds: the time of the maximum value of rain rates during cloud evolution T_{max} and the time of the first occurrence of a rain-rate value reaching

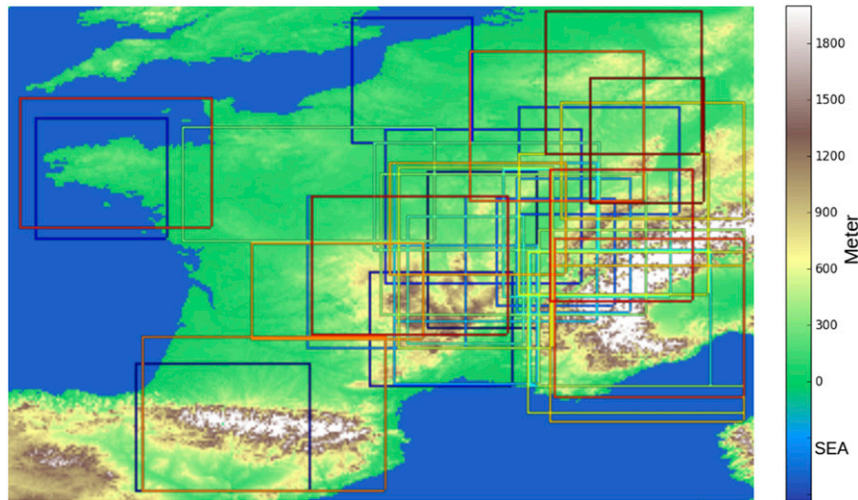


FIG. 6. Elevation map (shading) of France with tracking boxes of the 35 study cases (colored boxes).

an instantaneous threshold of $36 \text{ mm h}^{-1} T_{\text{thresh}}$. The synchronizations are performed on the maximum, minimum, median, first quartile (Q1), third quartile (Q3), and interquartile range (IQR) sequences by interpolating the variables onto two relative time scales: $T-T_{\text{max}}$ and $T-T_{\text{thresh}}$. This is similar to the approach used by Senf and Deneke (2017a). For each time step, a tracked cloud is associated with a precipitation area at the ground composed of a set of rain-rate values. In this study, we only consider the maximum value of this set of rain rates for each time step. Figure 7 shows the temporal evolution of the statistical distribution of these maximum values derived from the PANTHERE product for the tracked ensemble. The use of T_{thresh} and T_{max} is aimed at two different purposes. Time T_{thresh} is based on a fixed threshold of rain intensity and is suited for separation of periods of weak and high rain intensity (Fig. 7b). It allows for study of cloud evolution soon after precipitation onset at a stage where rainfall invigoration processes are likely to occur. Time T_{max} , on the other hand, is defined from the maximum in the rain-rate value and therefore marks the end of a period of increasing rain intensity (Fig. 7a).

Maximum rain rates are highly heterogeneous, with instantaneous values ranging between 36 and 180 mm h^{-1} at T_{max} (Fig. 7a). There are clear differences in the IQR during the -120 – 0 -min period shown in Fig. 7. For example, at -60 min the IQR is about 2.4 mm h^{-1} using T_{thresh} synchronization (Fig. 7b) while it is 25.2 mm h^{-1} using T_{max} synchronization (Fig. 7a). Differences can also be found in the evolution of extreme values. Maximum values reach 33.6 and 144 mm h^{-1} , respectively, for the T_{thresh} and T_{max} synchronizations. These differences are

explained by the heterogeneity of the rain period, rain intensity and tracking duration between study cases.

The cases among the total of 35 that are being tracked at any given time, relative to the T_{thresh} and T_{max} synchronization, are represented in Figs. 7c and 7d. Statistical distributions in Figs. 7a and 7b are calculated from these tracked cases. For example, the distribution of maximum values of rain rate calculated at -120 min using T_{max} synchronization is derived from 33 study cases (see Fig. 7c at -120 min). Clouds are tracked over periods with or without rain and the number of tracked cases exhibiting precipitation (not shown) is dependent on whether T_{max} and T_{thresh} is chosen. For example, at -90 min, 15 tracked clouds exhibit precipitation using T_{max} synchronization versus five clouds using T_{thresh} synchronization.

b. Analyzed mean of REFF, COT, CTT, and cloud-top phase

To assign an equal weight to each individually tracked cloud when performing analysis of temporal behavior of REFF, COT, and CTT of the ensemble, we first compute the mean values of these cloud properties for each tracked cloud system and then perform the time synchronization. Mean-value calculations depend on selection of the cloud area of interest in the tracking procedure. We consider cloud systems without any a priori selection of convective parts by using cloud-top temperature thresholding. In principle, this approach allows for the cloud-top phase transition to be observed at earlier stages so as to not track only cloud anvils.

Cloud phase classification from SEV06-CLD identifies each cloudy pixel as being either liquid water,

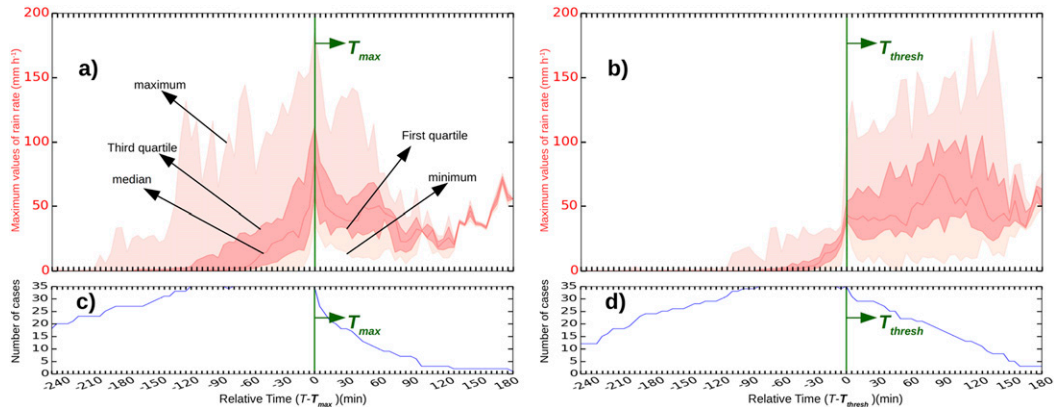


FIG. 7. Temporal behavior of maximum of rain-rate values for the 35 selected cases. Time scale is defined according to the chosen reference time. (a),(b) T_{\max} and T_{thresh} time synchronization, respectively; T_{\max} and T_{thresh} are represented by green vertical lines. The interquartile range and the area between the maximum and the minimum curves are colored in light red and pink, respectively. The red curve represents the median values. They are indicated by black arrows in (a). (c),(d) The evolution of the number of cases that are tracked relative to the T_{\max} time synchronization and T_{thresh} time synchronization, respectively.

undetermined phase, or ice phase. Manual inspection of this classification from SEV06-CLD alongside CTT evolution reveals that areas of rainfall are located close to parts of the tracked system with the coldest CTT, and either an ice or undetermined phase. This observation is supported by the temporal decrease in mean CTT prior to heavy rainfall (Fig. 8). At 1 h before T_{thresh} , the median of CTT distributions is approximately 279 K and it is approximately 260 K at T_{thresh} (Fig. 8b). Then, 1 h after T_{thresh} at +60 min, the median value is 245 K (Fig. 8b). It appears that the onset of heavy precipitation is associated with rapid cloud-top cooling. The same conclusion is obtained using T_{\max} temporal synchronization (Fig. 8a) although less clearly seen due to a higher IQR. Nonetheless, faster cloud-top cooling is associated with increasing rain intensity, consistent with previous cloud-top cooling observations (Negri and Adler 1981; Roberts and Rutledge 2003; Senf et al. 2015; Senf and Deneke 2017a).

Cloud-top phase classification is used to analyze mean ice REFF values separately. Figure 9 shows the fraction of ice REFF retrievals relative to total number of successful REFF retrievals (Figs. 9a,b), the mean ice crystal REFF (Figs. 9c,d), and mean ice cloud COT (Figs. 9e,f). From the percentage of ice REFF retrievals, there is an increase in the ice phase fractional area at cloud top concurrent with an increase in rain intensity. Median values for the fraction of ice (based on successful REFF retrievals) are greater than 50% after T_{thresh} and correspond to the occurrence of heavy rainfall at T_{\max} . While not surprising, this point illustrates the potential of such analysis for studies of the lead time between cloud-top glaciation and the onset of precipitation.

The temporal rate of change in the ice cloud fraction at cloud top retrieved using geostationary satellites has previously been used in a probabilistic model to assess the potential for the development of severe weather in developing convection (Cintineo et al. 2014). Moreover, Cintineo et al. (2013) have demonstrated that this parameter skillfully discriminates between severe and nonsevere events classified using weather reports of tornadoes and hail, but this study does not include a temporal analysis of precipitation during cloud life cycle. Although our analysis is not limited to the coldest convective parts of clouds, the ice REFF percentage distribution presented here confirms the occurrence of a glaciation period observed by previous studies of cloud anvils evolution (Senf et al. 2015; Senf and Deneke 2017a). The percentage of undetermined phase REFF retrievals (not shown) is not negligible. It is between 10% and 30% when ice REFF percentage increase and precipitation areas were not observed for clouds classified as liquid water clouds.

The mean REFF of ice clouds (Figs. 9c,d) is more challenging to interpret. Using the T_{thresh} synchronization, mean ice REFF Q1 and Q3 values are, respectively, 14 and 22 μm at -30 min and 19 and 24 μm at 0 min. For T_{\max} synchronization, the Q1-to-Q3 range is 18–26 μm at -30 min and 19–26 μm at 0 min. Relatively small ice crystals are observed 1 h before T_{thresh} and T_{\max} for at least half of the tracked cases (Figs. 9g,h). Median values of the mean CTT distribution (not plotted) associated with these ice crystals lie generally between 240 and 260 K at 30 min before both T_{\max} and T_{thresh} and between 230 and 240 K at 30 min after the two reference times.

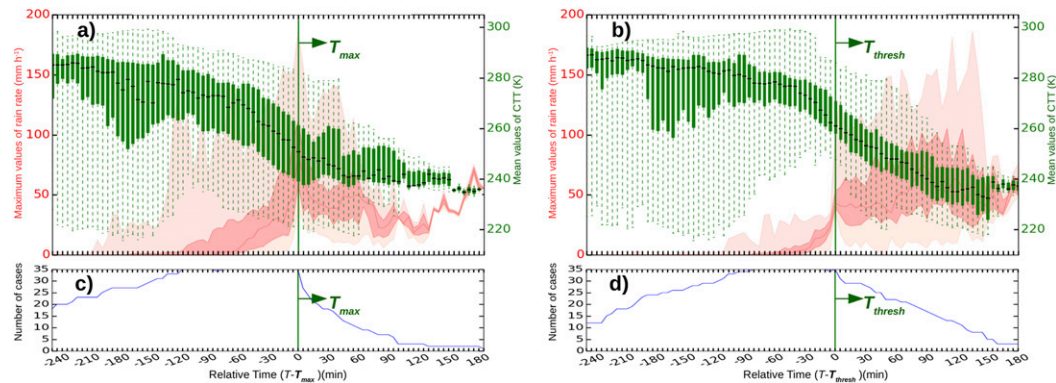


FIG. 8. Temporal evolution of box-and-whisker plot of mean of SAFNWC CTT for the 35 study cases. The interquartile range is represented by a green box where median values correspond to black lines and dotted vertical lines lie between the maximum and minimum of the distribution in the box-and-whisker plot representations. Maximum rainfall distribution of Fig. 7 is plotted in the background. (a) T_{thresh} time synchronization. (b) T_{max} time synchronization. (c), (d) As in Figs. 7c and 7d, respectively. From a statistical point of view, this is the number of cases used to construct the mean CTT distribution.

Observations of smaller ice crystals before T_{max} or T_{thresh} tend to be consistent with the hypothesis that stronger updrafts during the growth period of convective clouds lead to smaller ice crystals at cloud top (Rosenfeld et al. 2008; Senf et al. 2015; Mecikalski et al. 2016b; Senf and Deneke 2017a). An independent measure of updraft intensity would be needed to support this hypothesis even though cloud-top cooling can be used as a good proxy of updraft strength (Adler and Fenn 1979; Hamada and Takayabu 2016).

We have observed that there are increasing mean COT values over a 1-h period around T_{thresh} and T_{max} (Figs. 9e,f). Using the T_{thresh} synchronization, Q1 and Q3 values for mean ice COT are 6 and 13, respectively, at 30 min before T_{thresh} and 12 and 25 at 0 min. Using T_{max} synchronization, the Q1 and Q3 changes from 14 and 24, respectively, to 19 and 46 for the same period (Fig. 9e). Median values of the mean COT values continue to increase steadily until 40 min after T_{thresh} and 30 min after T_{max} . An increase in COT values has been observed in previous studies of convective clouds using alternative synchronization techniques (Senf et al. 2015; Mecikalski et al. 2011). In this work, mean values of COT and REFF associated with liquid water cloud-top phase classification have been calculated in a similar manner as in Fig. 9 (not shown). These distributions do not show particular temporal trends in the Q1 and Q3 values or median values relative to the T_{thresh} or T_{max} reference times. Nonetheless, increases in mean values of the described parameters generally correspond to higher rain intensities and to an increasing IQR. The IQR is generally higher for T_{max} synchronization than T_{thresh} synchronization.

c. Cloud perimeter-to-area ratio analysis

The study of CPAR is motivated by an analysis of mixing processes for cumulus convection. For plumes and thermals, the perimeter-to-area ratio is proportional to the inverse of radius (Squires and Turner 1962) and has been used as a starting point in entrainment and detrainment parameterizations (Turner 1963; Dawe and Austin 2013; de Rooy et al. 2013).

The pioneering work of Turner (1963) proposed that entrainment is proportional to the product of the cloud updraft velocity and the perimeter of the cloud horizontal cross section, yielding the result that the fractional entrainment at a given height is inversely proportional to the cloud radius (assuming that the cloud is cylindrical). Following de Rooy and Siebesma (2010) and de Rooy et al. (2013) [Eq. (10) in this paper] the entrainment rate per unit height is given by $\varepsilon = (P/A)(u/w)$, where P and A are, respectively, the perimeter and the area at a given height of the plume or thermal, w is the updraft velocity, and u is the net entrainment velocity across the perimeter. The ratio u/w is nearly constant although with different values for plumes and thermals, according to laboratory water tank experiments (Morton et al. 1956; Turner 1963). Thus, $\varepsilon \propto \text{CPAR}$. Low CPAR implies reduced entrainment that might mix dry stable air with the humid buoyant unstable air in clouds that is required for precipitation production. Effectively, the cores of clouds with low CPAR are more isolated per unit area from their clear-sky environment and should be expected to have a higher probability of intense precipitation production.

Clouds are neither pure plumes nor thermals, and mixing processes at cloud boundaries are complex

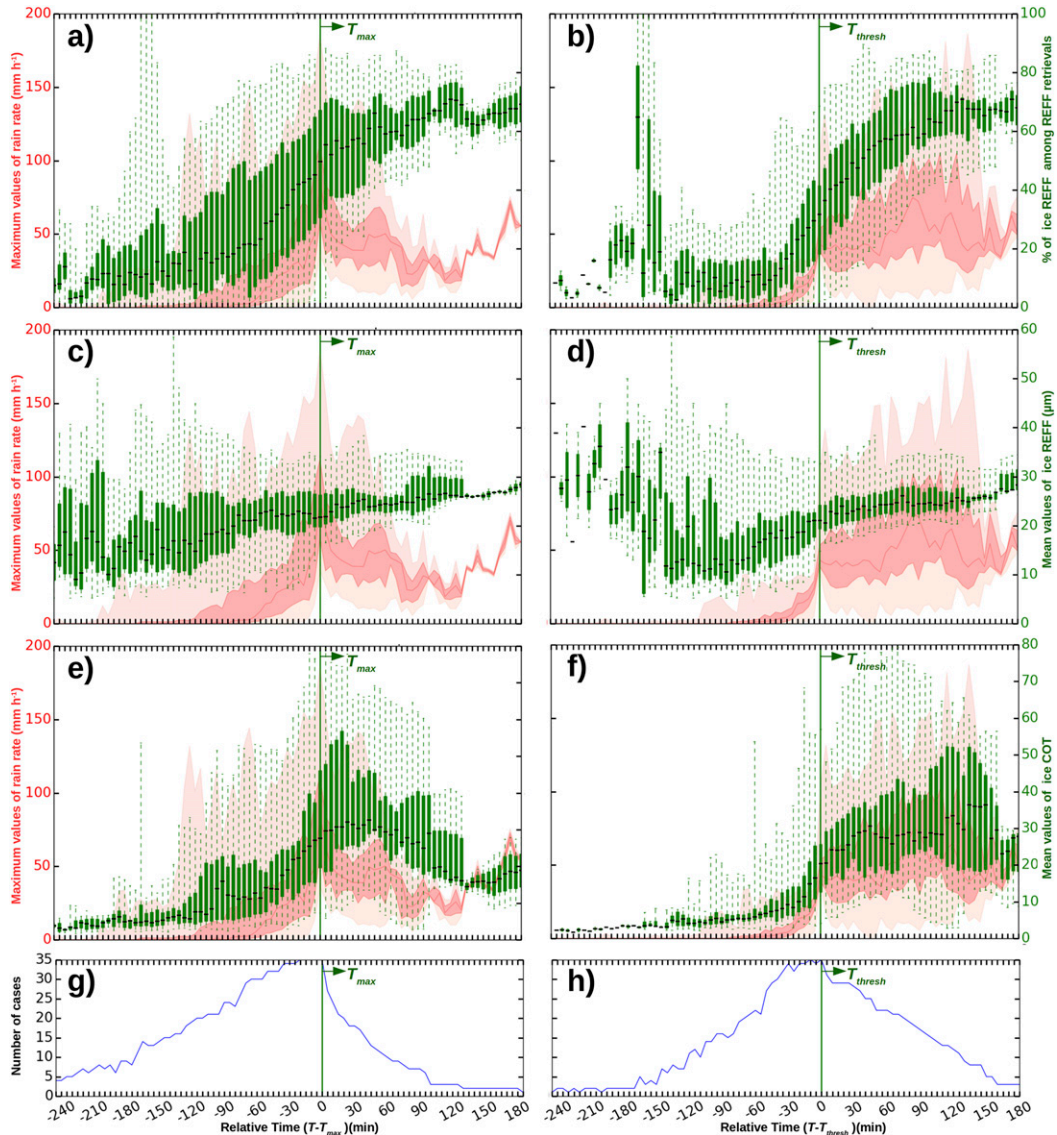


FIG. 9. As in Fig. 8, but for (a),(b) percentage values of REFF retrievals classified as ice crystals, (c),(d) mean ice REFF values, and (e),(f) mean ice COT values. (g),(h) The evolution of the number of cases presenting ice REFF and ice COT retrievals at cloud top. This is the number of cases among the 35 study cases involved in these statistical distributions. Note that these numbers are generally low during cloud life cycle because not all tracked clouds exhibit ice crystals at the same time. Synchronizations are with (left) T_{max} and (right) T_{thresh} as indicated by green arrows.

(Dawe and Austin 2013; de Rooy et al. 2013; Glenn and Krueger 2017). Despite these limitations, CPAR can be viewed as a measure of the overall magnitude of the mixing interface of a cloud system with its clear-sky surroundings. Small cumuli merge to form larger cells during thunderstorm development (Byers and Braham 1949), reducing CPAR and leading to increased probability of rain production (Sinkevich and Krauss 2014; Moseley et al. 2016).

Figure 10 shows box-and-whisker plots of CPAR for both T_{max} and T_{thresh} synchronization. For the 35 cases,

tracking quality indexes are less than 2 for at least 100 min prior to the chosen reference time. The Q1 and Q3 values of the CPAR distribution decrease over a period between 60 min before T_{thresh} when the median is 0.21 km^{-1} and 50 min after T_{thresh} when the median is 0.12 km^{-1} . A similar decrease is observed for the T_{max} reference but with more variation of the median values and a larger IQR: median values decrease from 0.21 to 0.13 km^{-1} between -80 and $+10$ min.

Periods of decreasing CPAR correspond to rain intensification and cloud-top glaciation (Fig. 9). The

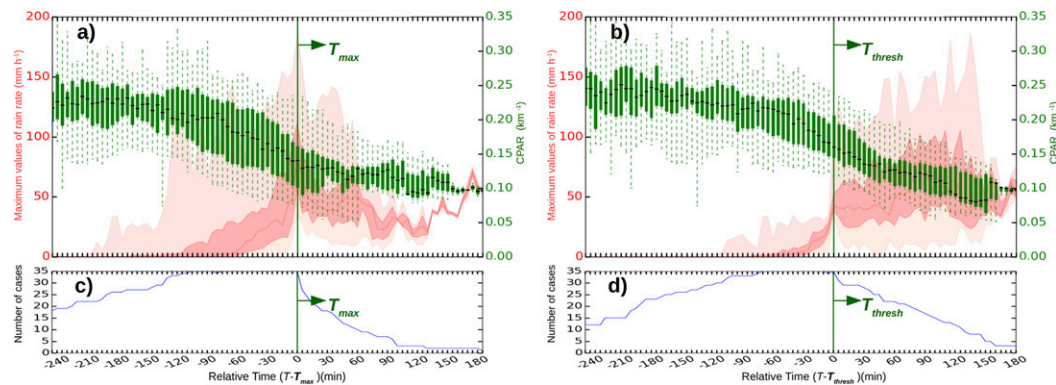


FIG. 10. As in Fig. 8, but for CPAR values: (a) T_{\max} synchronization, (b) T_{thresh} synchronization, and (c),(d) the evolution of the number of cases for which the CPAR calculation is feasible.

decreases in CPAR are particularly strong during the period of anvil formation and tend to be lowest when rain rates are highest. Figure 11 represents a scatterplot of the maximum of rain-rate values at T_{\max} as a function of the CPAR difference 30 min before and 30 min after T_{thresh} for 28 cases when this period is defined. This specific period of 1 h is not defined for five cases because of shorter tracking and rain periods. Figure 11 confirms that CPAR values decrease prior to intense rain for all of the 28 cases even if the maximum of rain rate at T_{\max} is very heterogeneous. Thus, it appears that decreasing CPAR could be a predictor of heavy rain onset.

d. RAMS simulations

We apply our cloud tracking and temporal analysis methodology to cloud-resolving model simulations over France. The purpose of this work is to analyze how convection in a cloud-resolving model impacts the CPAR values, mean ICE REFF values, cloud phase classification, and mean CTT values as well as to examine the feasibility of using our tracking methodology. To achieve this, we use the Colorado State University (CSU) Regional Atmospheric Modeling System (RAMS) (Cotton et al. 2003; Saleeby and van den Heever 2013), which is a state-of-the-art 3D non-hydrostatic Eulerian numerical research model developed and maintained by the van den Heever Group at the Colorado State University Department of Atmospheric Science.

Three idealized simulations were initialized within a horizontally homogeneous midlatitude environment as described by Weisman and Klemp (1982) and Takemi (2007). Horizontal resolution is 4 km. We consider a 100 pixel \times 100 pixel grid and the vertical resolution was stretched from 50 m close to the ground to 400 m in the upper troposphere on a total of 62 levels. We used

cyclic boundary conditions during the 6-h simulations. CSU RAMS uses a two-moment bulk microphysical parameterization scheme (Walko et al. 1995; Meyers et al. 1997; Saleeby and Cotton 2004) with eight hydrometeors (drizzle, cloud water, rain, pristine ice, snow, aggregates, graupel, and hail) that permit the representation in detail of the various microphysical processes: nucleation, freezing, vapor deposition, collection, coalescence, riming, sedimentation, melting, and collisional breakup. Weisman and Klemp (1982) used analytical functions to initialize vertical profiles of potential temperature θ_{env} and relative humidity (RH) of a typical midlatitude environment prior to the development of strong convective storms:

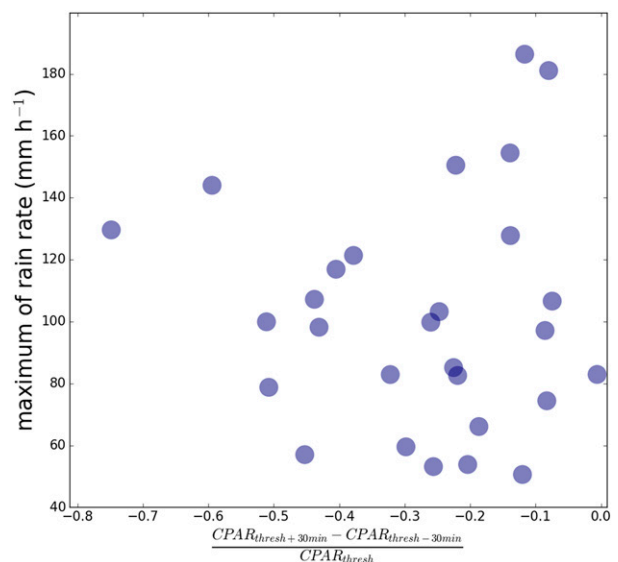


FIG. 11. Scatterplot of the maximum of rain-rate at T_{\max} as a function of the difference of CPAR at $T_{\text{thresh}} + 30 \text{ min}$ and $T_{\text{thresh}} - 30 \text{ min}$ standardized by the CPAR at T_{thresh} for 28 cases when the period from 30 min before to 30 min after T_{thresh} is defined.

$$\theta_{\text{env}}(z) = \begin{cases} \theta_0 + (\theta_{\text{tr}} - \theta_0) \left(\frac{z}{z_{\text{tr}}} \right)^{5/4}, & \text{where } z \leq z_{\text{tr}} \quad (1) \\ \theta_{\text{tr}}(z) \exp \left[\frac{g}{c_p T_{\text{tr}}} (z - z_{\text{tr}}) \right], & \text{where } z > z_{\text{tr}} \quad (2) \end{cases}$$

$$\text{RH}(z) = \begin{cases} 1 - 0.75 \left(\frac{z}{z_{\text{tr}}} \right)^{5/4}, & \text{where } z \leq z_{\text{tr}} \quad (3) \\ 0.25 - 2 \times 10^{-5} \times (z - z_{\text{tr}}), & \text{where } z > z_{\text{tr}} \quad (4) \end{cases}$$

where z_{tr} , T_{tr} , and θ_{tr} are the altitude, temperature, and potential temperature at the tropopause, respectively; θ_0 is the surface potential temperature. Here, we fixed identical environmental conditions for the three simulations. The surface temperature is set at 300 K, and the tropopause altitude at 12 km with a temperature and potential temperature of 213 and 343 K, respectively. Following Takemi (2007), the low-level moisture (below 1.5 km) was increased to a constant value of 16 g kg^{-1} in order to represent a well-mixed boundary layer. The westerly wind profile decreased from 10 m s^{-1} at the ground to 2 m s^{-1} at 2.5 km in altitude and was constant above. Therefore, the environmental convective available potential energy (CAPE) was 3600 J kg^{-1} for each of three simulations before triggering convection allowing us to focus the study on the impact of the convection triggering mechanism only. To create the ascent necessary to trigger deep convection, we introduced (i) a warm bubble for the first simulation, (ii) low-level wind convergence for the second simulation, and (iii) idealized orographic forcing for the third simulation. Each of these mechanisms has been adjusted to trigger deep convection within the same 64-km^2 geographic area and below 1.5 km in altitude. The warm bubble is represented by a perturbation of the potential temperature and moisture profiles of $+2 \text{ K}$ and $+10\%$, respectively, up to an altitude of 1.5 km and over a surface area of 64 km^2 . Low-level wind convergence (Loftus et al. 2008) is characterized by a divergence amplitude of -10^{-6} s^{-1} at the surface, linearly decreasing to zero at 1.5 km in altitude for an area of 64 km^2 . Orographic forcing is represented by a witch of Agnesi curve that mimics a 64-km^2 smooth hill shape reaching a maximum height at 1500-m altitude. We examine only cloud tops in the RAMS simulations to more closely mimic SEVIRI satellite observations. In RAMS, the layer corresponding to the cloud top is defined by a threshold of 0.02 g kg^{-1} on the water mixing ratio. When this threshold is reached (from top to bottom), the model layer between this level and the next one below is considered as the cloud top in

the analysis. REFF is retrieved using the parameterization of Wyser (1998). The cloud top is considered glaciated if the liquid water content of the cloud-top layer is 0 g m^{-3} .

Figure 12 shows the CPAR, the mean of the ice cloud REFF, the percentage of ice REFF retrievals at cloud top, and the mean of CTT for each of the three RAMS cloud simulations. Temporal synchronization of the simulations is based on time when the instantaneous rain rate reaches 36 mm h^{-1} similar to T_{thresh} used previously. We observed an increase in mean ice REFF. The percentage of ice crystals at cloud top increases toward 100% while mean CTT and CPAR decrease at the same time prior to the reference time (Fig. 12). This period is between 5 and 10 min, which is short compared to what is noted from satellite observations. However, RAMS simulations were not performed to establish a comparison with satellite observations, and the preconvective environment is not simulated. A direct comparison between RAMS simulations and SEVIRI observations would be very limited especially for ice REFF values. Indeed, we performed only three idealized simulations with the RAMS model and the hexagonal ice crystals habit assumption made in Wyser (1998) is different from the MODIS Collection 6 algorithm. Assumptions made for ice crystals can strongly impact the derived REFF values (Wyser 1998). How convection is triggered in the model can introduce differences in temporal evolution for the simulated parameters. A period of 10 min was found before complete glaciation occurred at the top of clouds (Fig. 12b) for the warm bubble simulation [denoted (i) in the key] and the orographic forcing simulation [denoted (iii) in the key]. The maximum of the rain rate is about 49 mm h^{-1} for the first simulation and $>100 \text{ mm h}^{-1}$ for the second simulation and is associated with larger mean ice crystals of $63 \mu\text{m}$ (Fig. 12d). These simulations show the potential of using similar cloud tracking techniques for observations and simulations especially for understanding the role of environmental conditions that trigger convection on rainfall enhancement.

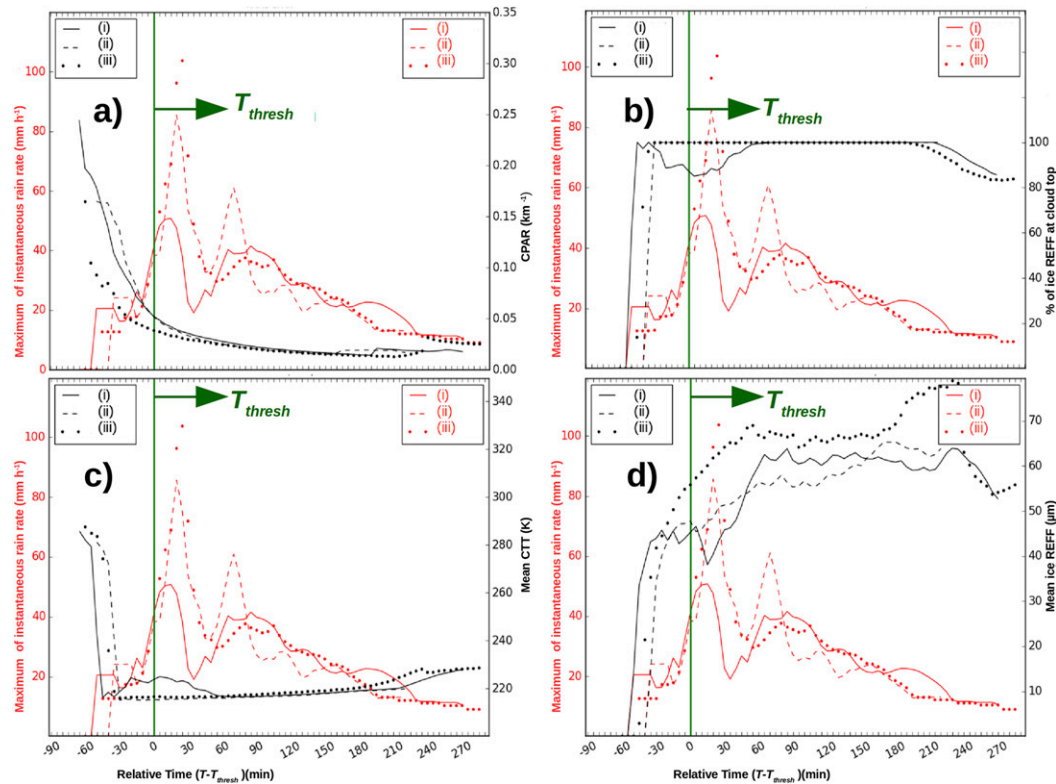


FIG. 12. Three RAMS idealized cloud simulations with different deep convection triggering. The legend indicates the triggering of convection used: (i) a warm bubble is used (solid lines), (ii) a low-level wind convergence is used (dashed lines), and (iii) an idealized orographic forcing is used (dotted lines). Red colored curves are the maximum of the instantaneous rain rate of simulated clouds. Black curves correspond to cloud-top parameters: (a) CPAR estimation, (b) percentage of ice REFF at cloud top, (c) mean of CTT, and (d) mean of ice REFF. All simulations are synchronized with T_{thresh} as indicated by green arrows.

4. Conclusions, limitations, and future prospects

In this study, we have developed a methodology to detect, track, select, and analyze the evolution of precipitating cloud systems during fair weather conditions over France. We analyzed 35 cases as a first step toward building a large database of rainfall events that includes cloud field properties observed by MSG/SEVIRI. We applied this tracking method to three RAMS simulations to illustrate how various convective triggering processes in models result in differing temporal evolution of the cloud properties that are observable by high-temporal-resolution geostationary satellites.

Our investigation has been restricted to a qualitative analysis of ice REFF, COT, CTT, cloud-top phase, and CPAR estimation for both simulations and study cases. The evolution of these parameters has been examined for convective cloud and storm characterization (Machado et al. 1998; Machado and Laurent 2004; Vila and Machado 2004; Mecikalski et al. 2011; Cintineo et al. 2013; Senf et al. 2015; Batista-Tomás et al. 2016;

Bley et al. 2016). In this work, we have considered mean values of REFF, CTT, and COT for each of the 35 tracked cloud systems without using a cloud-top temperature-based tracking technique. The cloud phase classification from the SEV06-CLD product is used to analyze separately the glaciated top of cloud for COT and REFF values. First, a tracking and detection procedure was introduced to identify isolated cloud trajectories from SEVIRI. Then, precipitating clouds were identified using a ground-based radar rain product. In addition, three RAMS model simulations of clouds have been presented to illustrate an application of our method to cloud-resolving model data. The temporal evolution of CPAR, mean of ice REFF, and cloud phase at cloud tops are observed prior to the onset of precipitation in RAMS simulations by changing the way deep convection is triggered.

For analysis of cloud property evolution, we introduced two reference times determined from the observed rain rates defined by a threshold of 36 mm h^{-1} (T_{thresh}) and by the time of maximum rain-rate value

during the cloud evolution (T_{\max}). The first of these times aimed at the study of the onset of precipitation at the early stages of cloud development and the second at the asymptotic behavior of cloud properties as they reach the point of a maximum rain intensity. These reference times have been defined to elucidate trends in observable cloud properties prior to heavy precipitation. Relative to the two reference times and from 35 synchronized cases, analysis of the evolution of averaged values toward T_{thresh} and T_{\max} shows the following:

- a period of growth and glaciation with a decrease of CPAR and mean CTT values and an increase in ice fraction at cloud top,
- smaller mean ice REFF values between 15 and $20 \mu\text{m}$, and
- an increase in mean COT values within the glaciated portion of the cloud top.

The choice in reference time used for synchronization of the 35 cases affects the calculated composite behavior of the cloud evolution. A smoother evolution of mean cloud properties and CPAR is observed when using for the reference time the time of first occurrence of the rain rate reaching 36 mm h^{-1} . The use of this reference time divides the tracked cloud life cycle into two distinct periods of weak rainfall and intense rainfall. It was found that CPAR decreases over a period of 2 h until the point of the maximum of rain rate during the cloud life cycle, suggesting that CPAR may be indicative of a “phase transition” in the cloud system from a non-precipitating to a precipitating state. Roebeling and Holleman (2009) have shown that REFF and COT can be indirectly used to estimate instantaneous rain rates. We observe that a period of increase of these parameters together with higher variability is indeed associated with rainfall intensity enhancement. We propose that higher heterogeneity in mean COT, mean REFF, and ice fraction during periods of heavy rain may be due to the disparity of the occurrence of significant rainfall between each case.

Our analysis is limited to 35 isolated cloud systems during daytime fair-weather conditions; Météo-France meteorological information and warnings indicate large numbers of strong rainfall events occurring at night. Mecikalski et al. (2013) previously showed that cirrus anvils in a preconvective environment are very common. This presents a limitation to the study of cloud-top evolution from space prior the onset of precipitation. The cloud cover used in our tracking technique is not adapted to properly detect multilayer situations and their respective cloud evolution. However, our methodology could easily be adapted for use with methods that employ

different binary cloud masks, cloud typing (Berendes et al. 2008), or overshooting top detection (Bedka et al. 2010; Bedka and Khlopenkov 2016). The data used in our paper are only available every 5 min; a higher resolution of 1 min would add significant information to study convective clouds (Mecikalski et al. 2016a).

We have also shown the feasibility of applying a satellite cloud tracking technique to the study of convective cloud top in idealized simulations. This work suggests new perspectives for comparing cloud-resolving model simulations and SEVIRI observations focusing on relating cloud dynamical processes such as strong updraft, entrainment, cloud vertical development, and to such cloud-top properties as CPAR, REFF, CTT, COT, and cloud phase. Another approach, not adopted here, could be to simulate SEVIRI radiances and derive cloud-top properties from those (Senf and Deneke 2017b). Future studies should explore a larger number of cases and simulations to evaluate the temporal evolution of cloud-top properties and CPAR as predictors of heavy rainfall periods.

Acknowledgments. This work was supported by the Programme National de Télédétection Spatiale (PNTS; <http://www.insu.cnrs.fr/pnts>), Grant PNTS-2016-12. SEVIRI cloud-type and cloud-top temperature data were obtained using the software from EUMETSAT’s Nowcasting and Very Short Range Forecasting Satellite Applications Facility (NWCSAF). We thank the ICARE Data and Services Center for providing development support and tools. We thank two anonymous reviewers and Hartwig Deneke, whose comments helped to improve this manuscript.

APPENDIX

Météo-France Daily Weather Reports and Regional Warnings

Météo-France daily reports reanalyses (DRR) and weather regional warnings (WRW) are manually analyzed if available near the tracked cloud systems. DRR is a reanalysis of daily France weather including temperature records and rain accumulation over 6 h. We use the DRR to perform a visualization of the 35 tracked cases mainly to check occurrences of storms, hail, and strong rainfall. There are four levels of Météo-France WRW. Level 1 indicates no potentially dangerous phenomena. Level 2 indicates potentially dangerous weather but not an unusual forecast. Level 3 indicates a dangerous forecast with unusual meteorological phenomena where damage and casualties are likely to happen. The maximum level is used when exceptionally

TABLE A1. Météo France weather, tracking time, rain period, and orography information of the 35 cases.

Case	Date	Mountainous area	DDR	Level of WRW	Tracking time (UTC)	Rain period (UTC)
1	23 Apr 2011	No	Thunderstorm	2	1355–1615	1505–1615
2	23 Apr 2011	No	Thunderstorm	2	1205–1530	1320–1530
3	24 Apr 2011	No	Thunderstorm	2	0955–1305	1200–1305
4	25 Apr 2011	No	Thunderstorm	2	0850–1305	1110–1305
5	27 Apr 2011	Yes	Unstable clouds	2	0845–1105	1005–1105
6	30 Apr 2011	Yes	Convective clouds	2	0800–1220	1025–1220
7	25 May 2012	Yes	Severe thunderstorm, hail	2	0800–1340	1215–1340
8	26 May 2012	Yes	Thunderstorm, hail, strong rain	2	1025–1410	1145–1410
9	26 May 2012	Yes	Thunderstorm, hail, strong rain	2	1005–1505	1140–1505
10	26 May 2012	Yes	Thunderstorm	2	0800–1650	1135–1650
11	28 Jun 2012	Yes	Thunderstorm	2	1155–1650	1405–1650
12	19 Aug 2012	Yes	Thunderstorm, strong rain	2	0800–1505	1150–1505
13	6 Jun 2013	Yes	Thundershower	2	0940–1430	1230–1430
14	6 Jun 2013	Yes	Thundershower	2	0800–1140	1025–1140
15	6 Jun 2013	Yes	—	2	0825–1310	1035–1310
16	7 Jun 2013	No	—	2	0810–1540	1125–1540
17	7 Jun 2013	No	Instability, rain	2	0945–1440	1220–1440
18	16 Jun 2013	Yes	Thunderstorm, wind	2	1020–1630	1255–1630
19	9 Apr 2014	Yes	Thunderstorm	2	0800–1230	1105–1230
20	10 Jun 2014	Yes	Thunderstorm	2	1135–1430	1230–1430
21	11 Jun 2014	Yes	Thundershower	2	0800–1300	1125–1300
22	12 Jun 2014	Yes	Thunderstorm	2	0915–1140	1110–1140
23	12 Jun 2014	Yes	Thunderstorm	2	0800–1315	1100–1315
24	12 Jun 2014	Yes	Thunderstorm	2	0800–1305	1115–1305
25	16 Jul 2014	Yes	Thunderstorm	—	0800–1205	0945–1205
26	24 Jul 2014	No	Thunderstorm	2	0800–1140	1005–1140
27	24 Jul 2014	Yes	Thunderstorm	2	0905–1245	1040–1245
28	5 Jun 2015	No	Local thunderstorm	2	1150–1655	1350–1655
29	5 Jun 2015	Yes	Thunderstorm	2	0800–1445	1200–1445
30	7 Aug 2015	Yes	Heat wave	2	0800–1640	1155–1640
31	23 Aug 2015	Yes	Moderate rain, wind	2	0800–1030	0800–1030
32	22 Jun 2016	Yes	Thunderstorm	1	0800–1635	1400–1635
33	15 Aug 2016	Yes	Thundershower	2	0905–1520	1205–1520
34	27 Aug 2016	No	—	—	0800–1345	1135–1345
35	27 Aug 2016	Yes	Thunderstorm	3	0925–1605	1240–1605

intense meteorological phenomena are confirmed. The Météo-France WRW does not only concern heavy rainfall. In addition, the warning scale is also issued in the event of such dangerous weather phenomena as strong winds, flooding, storms, or heatwaves. Classification of dangerous events is mainly based on weather forecaster analysis and seasonal average temperatures. Therefore, in WRW data, winds are considered dangerous if the mean intensity is more than 90 km h^{-1} . Hence, we have chosen to use the DDR and WRW only as a complement to rainfall product to check the occurrence of storm inside the tracking box. Temperature records of DDR indicate summer days for these 35 cases with maximum surface temperature exceeding 24°C in all cases. DDR data confirm the presence of thunderstorm, heavy rainfall, or hail near the tracked cloud objects. The majority of the 35 tracked cases are classified as level 2 of WRW. Case study tracking

periods, rain periods, and information from DDR and WRW are available in Table A1.

REFERENCES

- Adachi, A., T. Kobayashi, H. Yamauchi, and S. Onogi, 2013: Detection of potentially hazardous convective clouds with a dual-polarized C-band radar. *Atmos. Meas. Tech.*, **6**, 2741–2760, <https://doi.org/10.5194/amt-6-2741-2013>.
- Adler, R. F., and D. D. Fenn, 1979: Thunderstorm vertical velocities estimated from satellite data. *J. Atmos. Sci.*, **36**, 1747–1754, [https://doi.org/10.1175/1520-0469\(1979\)036<1747:TVVEFS>2.0.CO;2](https://doi.org/10.1175/1520-0469(1979)036<1747:TVVEFS>2.0.CO;2).
- Arnaud, Y., M. Desbois, and J. Maizi, 1992: Automatic tracking and characterization of African convective systems on Meteosat pictures. *J. Appl. Meteor.*, **31**, 443–453, [https://doi.org/10.1175/1520-0450\(1992\)031<0443:ATACOA>2.0.CO;2](https://doi.org/10.1175/1520-0450(1992)031<0443:ATACOA>2.0.CO;2).
- Batista-Tomás, A. R., O. Díaz, A. J. Batista-Leyva, and E. Althshuler, 2016: Classification and dynamics of tropical clouds by their fractal dimension. *Quart. J. Roy. Meteor. Soc.*, **142**, 983–988, <https://doi.org/10.1002/qj.2699>.

- Bedka, K. M., and K. Khlopenkov, 2016: A probabilistic multi-spectral pattern recognition method for detection of overshooting cloud tops using passive satellite imager observations. *J. Appl. Meteor. Climatol.*, **55**, 1983–2005, <https://doi.org/10.1175/JAMC-D-15-0249.1>.
- , J. Brunner, R. Dworak, W. Feltz, J. Otkin, and T. Greenwald, 2010: Objective satellite-based detection of overshooting tops using infrared window channel brightness temperature gradients. *J. Appl. Meteor. Climatol.*, **49**, 181–202, <https://doi.org/10.1175/2009JAMC2286.1>.
- Berendes, T. A., J. R. Mecikalski, W. M. MacKenzie, K. M. Bedka, and U. S. Nair, 2008: Convective cloud identification and classification in daytime satellite imagery using standard deviation limited adaptive clustering. *J. Geophys. Res.*, **113**, D20207, <https://doi.org/10.1029/2008JD010287>.
- Bley, S., H. Deneke, and F. Senf, 2016: Meteosat-based characterization of the spatiotemporal evolution of warm convective cloud fields over central Europe. *J. Appl. Meteor. Climatol.*, **55**, 2181–2195, <https://doi.org/10.1175/JAMC-D-15-0335.1>.
- Byers, H. R., and R. R. Braham, 1949: *The Thunderstorm: Report of the Thunderstorm Project*. U.S. Government Printing Office, 287 pp.
- Carvalho, L. M. V., and C. Jones, 2001: A satellite method to identify structural properties of mesoscale convective systems based on the maximum spatial correlation tracking technique (MASCOTTE). *J. Appl. Meteor.*, **40**, 1683–1701, [https://doi.org/10.1175/1520-0450\(2001\)040<1683:ASMTIS>2.0.CO;2](https://doi.org/10.1175/1520-0450(2001)040<1683:ASMTIS>2.0.CO;2).
- Cintineo, J. L., M. J. Pavolonis, J. M. Sieglaff, and A. K. Heidinger, 2013: Evolution of severe and nonsevere convection inferred from GOES-derived cloud properties. *J. Appl. Meteor. Climatol.*, **52**, 2009–2023, <https://doi.org/10.1175/JAMC-D-12-0330.1>.
- , —, —, and D. T. Lindsey, 2014: An empirical model for assessing the severe weather potential of developing convection. *Wea. Forecasting*, **29**, 639–653, <https://doi.org/10.1175/WAF-D-13-00113.1>.
- Cotton, W. R., and Coauthors, 2003: RAMS 2001: Current status and future directions. *Meteor. Atmos. Phys.*, **82**, 5–29, <https://doi.org/10.1007/s00703-001-0584-9>.
- Dawe, J. T., and P. H. Austin, 2013: Direct entrainment and detrainment rate distributions of individual shallow cumulus clouds in an LES. *Atmos. Chem. Phys.*, **13**, 7795–7811, <https://doi.org/10.5194/acp-13-7795-2013>.
- de Rooy, W. C., and P. A. Siebesma, 2010: Analytical expressions for entrainment and detrainment in cumulus convection. *Quart. J. Roy. Meteor. Soc.*, **136**, 1216–1227, <https://doi.org/10.1002/qj.640>.
- , and Coauthors, 2013: Entrainment and detrainment in cumulus convection: An overview. *Quart. J. Roy. Meteor. Soc.*, **139**, 1–19, <https://doi.org/10.1002/qj.1959>.
- Derrien, M., and H. Le Gléau, 2005: MSG/SEVIRI cloud mask and type from SAFNWC. *Int. J. Remote Sens.*, **26**, 4707–4732, <https://doi.org/10.1080/01431160500166128>.
- , and —, 2010: Improvement of cloud detection near sunrise and sunset by temporal-differencing and region-growing techniques with real-time SEVIRI. *Int. J. Remote Sens.*, **31**, 1765–1780, <https://doi.org/10.1080/01431160902926632>.
- Figueras i Ventura, J., and P. Tabary, 2013: The new French operational polarimetric radar rainfall rate product. *J. Appl. Meteor. Climatol.*, **52**, 1817–1835, <https://doi.org/10.1175/JAMC-D-12-0179.1>.
- Glenn, I. B., and S. K. Krueger, 2017: Connections matter: Updraft merging in organized tropical deep convection. *Geophys. Res. Lett.*, **44**, 7087–7094, <https://doi.org/10.1002/2017GL074162>.
- Hamada, A., and Y. N. Takayabu, 2016: Convective cloud top vertical velocity estimated from geostationary satellite rapid-scan measurements. *Geophys. Res. Lett.*, **43**, 5435–5441, <https://doi.org/10.1002/2016GL068962>.
- Heidinger, A. K., and M. J. Pavolonis, 2009: Gazing at cirrus clouds for 25 years through a split window. Part I: Methodology. *J. Appl. Meteor. Climatol.*, **48**, 1100–1116, <https://doi.org/10.1175/2008JAMC1882.1>.
- , —, R. E. Holz, B. A. Baum, and S. Berthier, 2010: Using CALIPSO to explore the sensitivity to cirrus height in the infrared observations from NPOESS/VIIRS and GOES-R/ABI. *J. Geophys. Res.*, **115**, D00H20, <https://doi.org/10.1029/2009JD012152>.
- Henken, C. C., M. J. Schmeits, H. Deneke, and R. A. Roebeling, 2011: Using MSG-SEVIRI cloud physical properties and weather radar observations for the detection of Cb/TCu Clouds. *J. Appl. Meteor. Climatol.*, **50**, 1587–1600, <https://doi.org/10.1175/2011JAMC2601.1>.
- ICARE/AERIS, 2017: Algorithm details: SEV06-CLD project. ICARE Data and Services Center, <https://dx.doi.org/10.25326/1>.
- Kolios, S., and H. Feidas, 2013: An automated nowcasting system of mesoscale convective systems for the Mediterranean basin using Meteosat imagery. Part I: System description. *Meteor. Appl.*, **20**, 287–295, <https://doi.org/10.1002/met.1282>.
- Le Gléau, H., 2016: Algorithm theoretical basis document for the cloud product processors of the NWC/GEO. Tech. Rep., EUMETSAT/SAFNWC/Météo France, 114 pp., <http://www.nwcsaf.org/web/guest/scientific-documentation>.
- Lensky, I. M., and D. Rosenfeld, 2006: The time–space exchangeability of satellite retrieved relations between cloud top temperature and particle effective radius. *Atmos. Chem. Phys.*, **6**, 2887–2894, <https://doi.org/10.5194/acp-6-2887-2006>.
- , and —, 2008: Clouds-Aerosols-Precipitation Satellite Analysis Tool (CAPSAT). *Atmos. Chem. Phys.*, **8**, 6739–6753, <https://doi.org/10.5194/acp-8-6739-2008>.
- Liu, J., C. Liu, X. Gu, and D. Qin, 2015: Detection of rapidly developing convection using rapid scan data from a geostationary satellite. *Remote Sens. Lett.*, **6**, 604–612, <https://doi.org/10.1080/2150704X.2015.1062160>.
- Loftus, A. M., D. B. Weber, and C. A. Doswell III, 2008: Parameterized mesoscale forcing mechanisms for initiating numerically simulated isolated multicellular convection. *Mon. Wea. Rev.*, **136**, 2408–2421, <https://doi.org/10.1175/2007MWR2133.1>.
- Lovejoy, S., 1982: Area–perimeter relation for rain and cloud areas. *Science*, **216**, 185–187, <https://doi.org/10.1126/science.216.4542.185>.
- Machado, L. A. T., and H. Laurent, 2004: The convective system area expansion over Amazonia and its relationships with convective system life duration and high-level wind divergence. *Mon. Wea. Rev.*, **132**, 714–725, [https://doi.org/10.1175/1520-0493\(2004\)132<0714:TCSAEO>2.0.CO;2](https://doi.org/10.1175/1520-0493(2004)132<0714:TCSAEO>2.0.CO;2).
- , W. B. Rossow, R. L. Guedes, and A. W. Walker, 1998: Life cycle variations of mesoscale convective systems over the Americas. *Mon. Wea. Rev.*, **126**, 1630–1654, [https://doi.org/10.1175/1520-0493\(1998\)126<1630:LCVOMC>2.0.CO;2](https://doi.org/10.1175/1520-0493(1998)126<1630:LCVOMC>2.0.CO;2).
- Maddox, R. A., 1980: Mesoscale convective complexes. *Bull. Amer. Meteor. Soc.*, **61**, 1374–1387, [https://doi.org/10.1175/1520-0477\(1980\)061<1374:MCC>2.0.CO;2](https://doi.org/10.1175/1520-0477(1980)061<1374:MCC>2.0.CO;2).
- Mathon, V., and H. Laurent, 2001: Life cycle of Sahelian mesoscale convective cloud systems. *Quart. J. Roy. Meteor. Soc.*, **127**, 377–406, <https://doi.org/10.1002/qj.49712757208>.
- McAnelly, R. L., and W. R. Cotton, 1989: The precipitation life cycle of mesoscale convective complexes over the central United States. *Mon. Wea. Rev.*, **117**, 784–808, [https://doi.org/10.1175/1520-0493\(1989\)117<0784:TPLCOM>2.0.CO;2](https://doi.org/10.1175/1520-0493(1989)117<0784:TPLCOM>2.0.CO;2).

- Mecikalski, J. R., and K. M. Bedka, 2006: Forecasting convective initiation by monitoring the evolution of moving cumulus in daytime GOES imagery. *Mon. Wea. Rev.*, **134**, 49–78, <https://doi.org/10.1175/MWR3062.1>.
- , —, S. J. Paech, and L. A. Litten, 2008: A statistical evaluation of GOES cloud-top properties for nowcasting convective initiation. *Mon. Wea. Rev.*, **136**, 4899–4914, <https://doi.org/10.1175/2008MWR2352.1>.
- , W. M. MacKenzie Jr., M. Koenig, and S. Muller, 2010a: Cloud-top properties of growing cumulus prior to convective initiation as measured by Meteosat Second Generation. Part I: Infrared fields. *J. Appl. Meteor. Climatol.*, **49**, 521–534, <https://doi.org/10.1175/2009JAMC2344.1>.
- , —, —, and —, 2010b: Cloud-top properties of growing cumulus prior to convective initiation as measured by Meteosat Second Generation. Part II: Use of visible reflectance. *J. Appl. Meteor. Climatol.*, **49**, 2544–2558, <https://doi.org/10.1175/2010JAMC2480.1>.
- , P. D. Watts, and M. Koenig, 2011: Use of Meteosat Second Generation optimal cloud analysis fields for understanding physical attributes of growing cumulus clouds. *Atmos. Res.*, **102**, 175–190, <https://doi.org/10.1016/j.atmosres.2011.06.023>.
- , P. Minnis, and R. Palikonda, 2013: Use of satellite derived cloud properties to quantify growing cumulus beneath cirrus clouds. *Atmos. Res.*, **120–121**, 192–201, <https://doi.org/10.1016/j.atmosres.2012.08.017>.
- , J. K. Williams, C. P. Jewett, D. Ahijevych, A. LeRoy, and J. R. Walker, 2015: Probabilistic 1-h convective initiation nowcasts that combine geostationary satellite observations and numerical weather prediction model data. *J. Appl. Meteor. Climatol.*, **54**, 1039–1059, <https://doi.org/10.1175/JAMC-D-14-0129.1>.
- , C. P. Jewett, J. M. Apke, and L. D. Carey, 2016a: Analysis of cumulus cloud updrafts as observed with 1-min resolution super rapid scan GOES imagery. *Mon. Wea. Rev.*, **144**, 811–830, <https://doi.org/10.1175/MWR-D-14-00399.1>.
- , D. Rosenfeld, and A. Manzato, 2016b: Evaluation of geostationary satellite observations and the development of a 1–2 h prediction model for future storm intensity. *J. Geophys. Res.*, **121**, 6374–6392, <https://doi.org/10.1002/2016JD024768>.
- Meyers, M. P., R. L. Walko, J. Y. Harrington, and W. R. Cotton, 1997: New RAMS cloud microphysics parameterization. Part II: The two-moment scheme. *Atmos. Res.*, **45**, 3–39, [https://doi.org/10.1016/S0169-8095\(97\)00018-5](https://doi.org/10.1016/S0169-8095(97)00018-5).
- Morel, C., and S. Senesi, 2002a: A climatology of mesoscale convective systems over Europe using satellite infrared imagery. I: Methodology. *Quart. J. Roy. Meteor. Soc.*, **128**, 1953–1971, <https://doi.org/10.1256/003590002320603485>.
- , and —, 2002b: A climatology of mesoscale convective systems over Europe using satellite infrared imagery. II: Characteristics of European mesoscale convective systems. *Quart. J. Roy. Meteor. Soc.*, **128**, 1973–1995, <https://doi.org/10.1256/003590002320603494>.
- Morton, B. R., F. R. S. Sir Geoffrey Taylor, and J. S. Turner, 1956: Turbulent gravitational convection from maintained and instantaneous sources. *Proc. Roy. Soc. London*, **234A**, 1–23, <https://doi.org/10.1098/rspa.1956.0011>.
- Moseley, C., C. Hohenegger, P. Berg, and J. O. Haerter, 2016: Intensification of convective extremes driven by cloud–cloud interaction. *Nat. Geosci.*, **9**, 748–752, <https://doi.org/10.1038/ngeo2789>.
- Nakajima, T., and M. D. King, 1990: Determination of the optical thickness and effective particle radius of clouds from reflected solar radiation measurements. Part I: Theory. *J. Atmos. Sci.*, **47**, 1878–1893, [https://doi.org/10.1175/1520-0469\(1990\)047<1878:DOTOTA>2.0.CO;2](https://doi.org/10.1175/1520-0469(1990)047<1878:DOTOTA>2.0.CO;2).
- Negri, A. J., and R. F. Adler, 1981: Relation of satellite-based thunderstorm intensity to radar-estimated rainfall. *J. Appl. Meteor.*, **20**, 288–300, [https://doi.org/10.1175/1520-0450\(1981\)020<0288:ROSBTI>2.0.CO;2](https://doi.org/10.1175/1520-0450(1981)020<0288:ROSBTI>2.0.CO;2).
- Platnick, S., J. Y. Li, M. D. King, H. Gerber, and P. V. Hobbs, 2001: A solar reflectance method for retrieving the optical thickness and droplet size of liquid water clouds over snow and ice surfaces. *J. Geophys. Res.*, **106**, 15 185–15 199, <https://doi.org/10.1029/2000JD900441>.
- , M. D. King, S. A. Ackerman, W. P. Menzel, B. A. Baum, J. C. Riedi, and R. A. Frey, 2003: The MODIS cloud products: Algorithms and examples from Terra. *IEEE Trans. Geosci. Remote Sens.*, **41**, 459–473, <https://doi.org/10.1109/TGRS.2002.808301>.
- , and Coauthors, 2017: The MODIS cloud optical and microphysical products: Collection 6 updates and examples from Terra and Aqua. *IEEE Trans. Geosci. Remote Sens.*, **55**, 502–525, <https://doi.org/10.1109/TGRS.2016.2610522>.
- Renard, F., P.-M. Chapon, and J. Comby, 2012: Assessing the accuracy of weather radar to track intense rain cells in the Greater Lyon area, France. *Atmos. Res.*, **103**, 4–19, <https://doi.org/10.1016/j.atmosres.2011.08.008>.
- Roberts, R. D., and S. Rutledge, 2003: Nowcasting storm initiation and growth using GOES-8 and WSR-88D data. *Wea. Forecasting*, **18**, 562–584, [https://doi.org/10.1175/1520-0434\(2003\)018<0562:NSIAGU>2.0.CO;2](https://doi.org/10.1175/1520-0434(2003)018<0562:NSIAGU>2.0.CO;2).
- Roca, R., T. Fiolleau, and D. Bouniol, 2017: A simple model of the life cycle of mesoscale convective systems cloud shield in the tropics. *J. Climate*, **30**, 4283–4298, <https://doi.org/10.1175/JCLI-D-16-0556.1>.
- Roebeling, R. A., and I. Holleman, 2009: SEVIRI rainfall retrieval and validation using weather radar observations. *J. Geophys. Res.*, **114**, D21202, <https://doi.org/10.1029/2009JD012102>.
- Rosenfeld, D., W. L. Woodley, A. Lerner, G. Kelman, and D. T. Lindsey, 2008: Satellite detection of severe convective storms by their retrieved vertical profiles of cloud particle effective radius and thermodynamic phase. *J. Geophys. Res.*, **113**, D04208, <https://doi.org/10.1029/2007JD008600>.
- Saleeby, S. M., and W. R. Cotton, 2004: A large-droplet mode and prognostic number concentration of cloud droplets in the Colorado State University Regional Atmospheric Modeling System (RAMS). Part I: Module descriptions and supercell test simulations. *J. Appl. Meteor.*, **43**, 182–195, [https://doi.org/10.1175/1520-0450\(2004\)043<0182:ALMAPN>2.0.CO;2](https://doi.org/10.1175/1520-0450(2004)043<0182:ALMAPN>2.0.CO;2).
- , and S. C. van den Heever, 2013: Developments in the CSU-RAMS aerosol model: Emissions, nucleation, regeneration, deposition, and radiation. *J. Appl. Meteor. Climatol.*, **52**, 2601–2622, <https://doi.org/10.1175/JAMC-D-12-0312.1>.
- Schmetz, J., P. Pili, S. Tjemkes, D. Just, J. Kerkmann, S. Rota, and A. Ratier, 2002: An introduction to Meteosat Second Generation (MSG). *Bull. Amer. Meteor. Soc.*, **83**, 977–992, [https://doi.org/10.1175/1520-0477\(2002\)083<0977:AITMSG>2.3.CO;2](https://doi.org/10.1175/1520-0477(2002)083<0977:AITMSG>2.3.CO;2).
- Senf, F., and H. Deneke, 2017a: Satellite-based characterization of convective growth and glaciation and its relationship to precipitation formation over central Europe. *J. Appl. Meteor. Climatol.*, **56**, 1827–1845, <https://doi.org/10.1175/JAMC-D-16-0293.1>.
- , and —, 2017b: Uncertainties in synthetic Meteosat SEVIRI infrared brightness temperatures in the presence

- of cirrus clouds and implications for evaluation of cloud microphysics. *Atmos. Res.*, **183**, 113–129, <https://doi.org/10.1016/j.atmosres.2016.08.012>.
- , F. Dietzsch, A. Hünnerbein, and H. Deneke, 2015: Characterization of initiation and growth of selected severe convective storms over central Europe with MSG-SEVIRI. *J. Appl. Meteor. Climatol.*, **54**, 207–224, <https://doi.org/10.1175/JAMC-D-14-0144.1>.
- Sieglauff, J. M., L. M. Counce, W. F. Feltz, K. M. Bedka, M. J. Pavolonis, and A. K. Heidinger, 2011: Nowcasting convective storm initiation using satellite-based box-averaged cloud-top cooling and cloud-type trends. *J. Appl. Meteor. Climatol.*, **50**, 110–126, <https://doi.org/10.1175/2010JAMC2496.1>.
- , —, and —, 2014: Improving satellite-based convective cloud growth monitoring with visible optical depth retrievals. *J. Appl. Meteor. Climatol.*, **53**, 506–520, <https://doi.org/10.1175/JAMC-D-13-0139.1>.
- Sinkevich, A. A., and T. W. Krauss, 2014: Changes in thunderstorm characteristics due to feeder cloud merging. *Atmos. Res.*, **142**, 124–132, <https://doi.org/10.1016/j.atmosres.2013.06.007>.
- Squires, P., and J. S. Turner, 1962: An entraining jet model for cumulo-nimbus updraughts. *Tellus*, **14**, 422–434, <https://doi.org/10.3402/tellusa.v14i4.9569>.
- Tabary, P., 2007: The new French operational radar rainfall product. Part I: Methodology. *Wea. Forecasting*, **22**, 393–408, <https://doi.org/10.1175/WAF1004.1>.
- , J. Desplats, K. D. Khac, F. Eidelman, C. Gueguen, and J.-C. Heinrich, 2007: The new French operational radar rainfall product. Part II: Validation. *Wea. Forecasting*, **22**, 409–427, <https://doi.org/10.1175/WAF1005.1>.
- Takemi, T., 2007: Environmental stability control of the intensity of squall lines under low-level shear conditions. *J. Geophys. Res.*, **112**, D24110, <https://doi.org/10.1029/2007JD008793>.
- Turner, J. S., 1963: The motion of buoyant elements in turbulent surroundings. *J. Fluid Mech.*, **16**, 1–16, <https://doi.org/10.1017/S0022112063000549>.
- van der Walt, S., and Coauthors, 2014: scikit-image: Image processing in Python. 19 pp., <http://arxiv.org/abs/1407.6245>.
- Vila, D., and L. Machado, 2004: Shape and radiative properties of convective systems observed from infrared satellite images. *Int. J. Remote Sens.*, **25**, 4441–4456, <https://doi.org/10.1080/01431160410001726085>.
- , —, H. Laurent, and I. Velasco, 2008: Forecast and Tracking the Evolution of Cloud Clusters (ForTraCC) using satellite infrared imagery: Methodology and validation. *Wea. Forecasting*, **23**, 233–245, <https://doi.org/10.1175/2007WAF2006121.1>.
- Walko, R., W. Cotton, M. Meyers, and J. Harrington, 1995: New RAMS cloud microphysics parameterization. Part I: The single-moment scheme. *Atmos. Res.*, **38**, 29–62, [https://doi.org/10.1016/0169-8095\(94\)00087-T](https://doi.org/10.1016/0169-8095(94)00087-T).
- Weisman, M. L., and J. B. Klemp, 1982: The dependence of numerically simulated convective storms on vertical wind shear and buoyancy. *Mon. Wea. Rev.*, **110**, 504–520, [https://doi.org/10.1175/1520-0493\(1982\)110<0504:TDONSC>2.0.CO;2](https://doi.org/10.1175/1520-0493(1982)110<0504:TDONSC>2.0.CO;2).
- Wolters, E. L. A., R. A. Roebeling, and A. J. Feijt, 2008: Evaluation of cloud-phase retrieval methods for SEVIRI on *Meteosat-8* using ground-based lidar and cloud radar data. *J. Appl. Meteor. Climatol.*, **47**, 1723–1738, <https://doi.org/10.1175/2007JAMC1591.1>.
- Wu, K., E. Otoo, and A. Shoshani, 2005: Optimizing connected component labeling algorithms. Lawrence Berkeley National Laboratory, 13 pp., <http://www.escholarship.org/uc/item/7jg5d1zn>.
- Wyser, K., 1998: The effective radius in ice clouds. *J. Climate*, **11**, 1793–1802, [https://doi.org/10.1175/1520-0442\(1998\)011<1793:TERIIC>2.0.CO;2](https://doi.org/10.1175/1520-0442(1998)011<1793:TERIIC>2.0.CO;2).
- Zhang, Z., and S. Platnick, 2011: An assessment of differences between cloud effective particle radius retrievals for marine water clouds from three MODIS spectral bands. *J. Geophys. Res.*, **116**, D20215, <https://doi.org/10.1029/2011JD016216>.
- , A. S. Ackerman, G. Feingold, S. Platnick, R. Pincus, and H. Xue, 2012: Effects of cloud horizontal inhomogeneity and drizzle on remote sensing of cloud droplet effective radius: Case studies based on large-eddy simulations. *J. Geophys. Res.*, **117**, D19208, <https://doi.org/10.1029/2012JD017655>.
- Zinner, T., H. Mannstein, and A. Tafferner, 2008: Cb-TRAM: Tracking and monitoring severe convection from onset over rapid development to mature phase using multi-channel *Meteosat-8* SEVIRI data. *Meteor. Atmos. Phys.*, **101**, 191–210, <https://doi.org/10.1007/s00703-008-0290-y>.